frontiers in Physics

ORIGINAL RESEARCH
published: 08 April 2020
doi: 10.3389/fphy.2020.00066

A New Computational Technique Design for EMHD Nanofluid Flow Over a Variable Thickness Surface With Variable Liquid Characteristics

Muhammad Irfan, Muhammad Asif Farooq and Tousif Iqra*

Department of Mathematics, School of Natural Sciences (SNS), National University of Sciences and Technology (NUST), Islamabad, Pakistan

The objective of this paper comprises two key aspects: to establish descriptive mathematical models for constant and variable fluid flows over a variable thickness sheet by inducting applied electric and magnetic fields, porosity, radiative heat transfer, and heat generation/absorption, and to seek their solution by constructing a novel numerical method, the Simplified Finite Difference Method (SFDM). We resort to similarity transformations to implicate partial differential equations (PDEs) into a set of ordinary differential equations (ODEs). Optimal results for a pair of ODEs obtained from SFDM are assessed by drawing a comparison with *bvp4c* and existing literature values. SFDM has been implemented in MATLAB for both constant and variable fluid properties. Tabulated numerical values of the skin friction coefficient and local Nusselt and Sherwood numbers are measured and analyzed against different parameters. The influence of distinct parameters on velocity, temperature, and nanoparticle volume fraction are explained in great detail via diagrams. The skin friction coefficient for variable fluid properties is greater than for constant fluid properties. However, the local Nusselt number is lower for variable fluid properties than with constant fluid properties. Surprisingly, high-precision computational results are achieved from the SFDM.

Keywords: electrical magnetohydrodynamics (EMHD), variable thicked surface, nanofluid, simplified finite difference method (SFDM), variable fluid properties

OPEN ACCESS

Edited by:
Muhammad Mubashir Bhatti, Shanghai University, China

Reviewed by:
Rahmat Ellahi, University of California, Riverside, United States
Muhammad Ibrahim, University of Science and Technology Beijing, China

****Correspondence:***
Muhammad Asif Farooq
asiffarooq.2007@gmail.com

Specialty section:
This article was submitted to Mathematical Physics, a section of the journal Frontiers in Physics

Received: *02 December 2019*
Accepted: *28 February 2020*
Published: *08 April 2020*

Citation:
Irfan M, Farooq MA and Iqra T (2020) A New Computational Technique Design for EMHD Nanofluid Flow Over a Variable Thickness Surface With Variable Liquid Characteristics. Front. Phys. 8:66. doi: 10.3389/fphy.2020.00066

1. INTRODUCTION

Fluid mechanics has many applications in contexts from the human biological system to the manufacturing industry. For example, the study of breathing in biological systems uses bio-fluid dynamics. Cooling is another such phenomenon, which is important in electronics and the automobile industry. Investigating stretching sheet flows is relevant to many significant applications. All of this plays a vital role in technological advances such as those of polymer manufacturing and cooling processes in glass and paper production Hayat et al. [1]. Having variable thickness becomes useful in minimizing the weight of architectural elements Hayat et al. [1].

Hayat et al. [1, 2] analyzed the consequences of Cattaneo-Christov heat flux and a temperature-dependent fluid thermal conductivity on fluid flow over a variable thickness sheet and showed that variable conductivity enhances the temperature distribution. They also maintained that the temperature profile decreases with the thermal relaxation parameter. Mabood et al. [3] discussed the non-Darcian MHD convective flow and claimed that temperature rise depends on the Eckert

number. In the context of a stretching sheet for variable thickness, Fang et al. [4] has tackled the boundary layer flow and analyzed multiple solutions. Khader and Ahmed [5] computed a numerical solution for variable sheet thickness with slip velocity and pointed out that the skin friction coefficient increases with the wall thickness parameter. Daniel et al. [6] discussed the thermal stratification effects on MHD radiative flow of nanofluid for a variable thickness sheet. They submitted that the thermal stratification effect reduces temperature. Reddy et al. [7] investigated the MHD flow and heat transfer of Williamson nanofluid over a variable thickness sheet with variable thermal conductivity and identified that the velocity profile decreases with the wall thickness parameter when $m < 1$. Daniel et al. [8] examined the effect of thermal radiation on electrical MHD flow of nanofluid over a stretching sheet with variable thickness and concluded that the thermal radiation did impact the nanofluid temperature.

Magnetohydrodynamics is the study of the flow of electrically conducting fluids in an electro-magnetic-field. The study of MHD flow is of considerable interest in modern metallurgical and metal-working processes. Noreen et al. [9] examined the numerical solutions of magnetohydrodynamic boundary layer flow of tangent hyperbolic fluid toward a stretching sheet. They showed that the skin friction coefficient increases with an increase in M. Mukhopadhyay et al. [10] conducted a study to assess the effects of fluid flow with constant and changeable viscosity on a heated surface. They noticed that a decrease in viscosity causes the velocity to decrease with increasing distance along the stretching sheet. Nadeem et al. [11] examined MHD three-dimensional Casson fluid flow through a porous linear stretching plate and concluded that the stretching parameter resulted in decreasing behavior of the velocity profile. Mabood et al. [12] investigated MHD boundary layer flow and heat transfer of nanofluid over a non-linear stretching sheet. They note that the boundary layer thickness grows with Brownian motion. Zhang et al. [13] discussed the MHD flow and radiation heat transfer of nanofluids in porous media with variable surface heat flux and chemical reaction. They examined three types of nanoparticles. Popley et al. [14] addressed the overall impact of varying liquid characteristics upon hydro-magnetic motion and heat transfer across a non-linear stretching surface. They demonstrated that the free stream velocity induces a reduction in the boundary layer thickness. Mohsen et al. [15] discussed nanofluid flow with convective heat transfer considering Lorentz forces and showed that heat transfer rises with the Hartmann number. Patel [16] studied the effects of heat generation, thermal radiation, and Hall current on MHD Casson fluid flow past an osculating plate in a porous medium. They stated that the Hall current boosts mobility in both directions. Farooq et al. [17] discussed the MHD flow of Maxwell fluid with nanomaterials due to an exponentially stretching surface. The influence of the thermophoresis parameter on the temperature distribution is negligible. Magnetohydrodynamic (MHD) boundary layer flow past a wedge with heat transfer and viscous effects of nanofluid embedded in porous media was investigated by Ibrahim and Tulu [18]. They discover that the pressure gradient influences the boundary layer thickness. The impact of 3D Maxwell nanofluid flow over an exponentially stretching surface in terms of heat and mass transfer was explored by Ali et al. [19]. They showed that the skin friction coefficient decreases with the Deborah number.

Nanofluids solid-liquid suspensions consisting of solid nanoparticles of size 1-100 nm and liquid Mabood et al. [3]. Due to reports of their having significantly enhanced thermal properties, nanofluids have drawn great interest recently Mabood et al. [3]. The term nanofluid was proposed by Choi and Eastman [20], who demonstrated that the introduction of a small number of nanoparticles (< 1 percent by volume fraction) to traditional liquids increased the fluid thermal conductivity by approximately two times Nadeem et al. [11]. The numerical simulation of nanofluid flow with convective boundary conditions was studied by Das et al. [21], who demonstrated that the surface convection parameter enhances the heat transfer rate. Mabood and Das [22], in their analysis, communicated melting heat transfer of hydromagnetic nanofluid flow with a second-order slip condition. Cao et al. [23] discussed the MHD flow and heat transfer of fractional Maxwell viscoelastic nanofluid over a moving plate by using a finite difference method and found that the average Nusselt number is higher with a rise in the fractional derivative parameter. Das et al. [24] studied the effects of a magnetic field on an unsteady mixed convection flow of nanofluids containing spherical and cylindrical nanoparticles. Narayana et al. [25] discussed the effects of thermal radiation and a heat source on an MHD nanofluid past a vertical plate in a rotating system with a porous medium. They used three different nanoparticles and showed that they enhance the heat transfer rate, a result that can be used in heat exchanger technology. The influences on stagnation-point flow toward a stretching/shrinking sheet in a nanofluid were discussed by Mansur et al. [26] using the Buongiorno model. They proved that the thermophoresis parameter reduces the heat transfer rate. Makinde [27] studied viscous dissipation and Newtonian heating over a flat plate in a nanofluid. The heat transfer rate rises with the nanoparticle volume fraction and the Biot number. Ali et al. [28] discussed a numerical study of unsteady MHD Couette flow and heat transfer of nanofluids in a rotating system with convective cooling and indicated that the rotation has a significant effect on velocity and heat transfer. Ashwinkumar and Sulochana [29] investigated the effect of radiation absorption and buoyancy force on the MHD mixed convection flow of Casson nanofluid. They noticed that the volume fraction of nanoparticles governs the temperature distribution. Under temperature control, Andersson and Aarseth [30] revisited the fluid properties of a liquid. The effect of variable fluid properties on the hydromagnetic flow and heat transfer over a non-linearly stretching sheet was discussed by Prasad et al. [31]. Hayat et al. [32] discussed mixed convection flow across a porous sheet and reported that the thermal boundary layer thickness is lowered with Pr. Reddy et al. [33] probed the effect of variable thermal conductivity on MHD flow of nanofluid over a stretching sheet. They considered convective boundary conditions. Zaka et al. [34] applied numerical simulation for Darcy-Forchheimer flow of nanofluid by considering a rotating disk. They reported that the temperature distribution is enhanced with the thermophoresis parameter. Shah et al. [35] discussed the nanofluid flow for

different shape factors. They managed to show that the shape factor causes stronger convection. Zeeshan et al. [36] reported the effect of radiative nanofluid flow under a pressure gradient due to entropy generation and observed an increase in entropy with an increase in the pressure gradient. Ellahi et al. [37] investigated flow of a power-law nanofluid with entropy generation and noted that the skin friction coefficient increases at the heated wall. Yousif et al. [38] analyzed the momentum and heat transfer of MHD Carreau nanofluid over an exponentially stretching surface and used the shooting method to compute the solution. Sarafraz et al. [39] discussed the pool boiling heat transfer characteristics of an iron oxide nano-suspension considering a constant magnetic field and found that bubble formation is intensified due to the magnetic field. Fujimoto [40] described multi-scale simulation on adaptive meshes.

This paper is arranged in the following way. A mathematical formalism of the physical model is explained in section Problem Formulation. Section Fluid Properties Analysis addresses constant as well as varying liquid characteristics. Section Physical Quantities provides physical quantities, and an overview of the numerical process has been given in section Numerical Procedure. Results and discussion are presented in section Result and Discussion. In section Conclusions, the conclusion is drawn.

2. PROBLEM FORMULATION

We assume an electrical magnetohydrodynamic (EMHD), two-dimensional, steady, laminar flow of nanofluid over a non-linear stretching sheet with variable thickness. A variable magnetic field $B(x) = B_o(x+b)^{\frac{n-1}{2}} (n \neq 1)$ and variable electrical field $E(x) = E_o(x+b)^{\frac{n-1}{2}} (n \neq 1)$ are applied normal to the direction of flow. The sheet is stretching with non-linear velocity $U_w = U_o(x+b)^n (n \neq 1)$, where b is the dimensional constant and U_o is the reference velocity. Therefore, the surface is considered not to be flat, and its thickness varies as $y = A(x+b)^{\frac{1-n}{2}} (n \neq 1)$, where A is a very small constant to hold the sheet thin enough. We also observe that for $n = 1$, the current problem reduces to a flat sheet. The geometry of the problem is shown in **Figure 1**, where the x-axis has been taken along the sheet and y-axis is normal to it.

The induced magnetic field has been neglected under the assumption of a small magnetic Reynolds number. The boundary layer equations governing this flow are Daniel et al. [6, 8] and Irfan et al. [41]

$$\frac{\partial u}{\partial x} + \frac{\partial v}{\partial y} = 0, \tag{1}$$

$$u\frac{\partial u}{\partial x} + v\frac{\partial u}{\partial y} = \frac{1}{\rho}\frac{\partial}{\partial y}(\frac{\mu \partial u}{\partial y}) + \frac{\sigma}{\rho}(E(x)B(x) - B^2(x)u) - \frac{\mu}{\rho K(x)}u \tag{2}$$

$$u\frac{\partial T}{\partial x} + v\frac{\partial T}{\partial y} = \frac{1}{\rho C_p}\frac{\partial}{\partial y}(\frac{k\partial T}{\partial y}) + \tau(D_B\frac{\partial T}{\partial y}\frac{\partial C}{\partial y} + \frac{D_T}{T_\infty}(\frac{\partial T}{\partial y})^2)$$
$$-\frac{1}{\rho C_p}\frac{\partial q_r}{\partial y} + \frac{\sigma}{\rho C_p}(uB(x) - E(x))^2 + \frac{Q(x)}{\rho C_p}(T - T_\infty), \tag{3}$$

$$u\frac{\partial C}{\partial x} + v\frac{\partial C}{\partial y} = D_B\frac{\partial^2 C}{\partial y^2} + \frac{D_T}{T_\infty}\frac{\partial^2 T}{\partial y^2}, \tag{4}$$

Here, u and v are the velocity components parallel to the $x-$ and $y-$ axis, respectively. Further, μ is the viscosity, ρ is the density, ν is the kinematic viscosity, C_p is the specific heat capacity, B is the magnetic field. T and C are the fluid temperature and nanoparticle fraction, respectively. The temperature of the fluid at the wall and ambient temperature are denoted by T_w and T_∞, respectively. D_B and D_T are the Brownian diffusion coefficient and thermophoretic diffusion coefficient, respectively. $\tau = \frac{(\rho c)_p}{(\rho c)_f}$ is the ratio of the effective heat capacity of the nanoparticle material to the heat capacity of the fluid, q_r is the radiative heat flux, $Q(x) = Q_0(x+b)^{\frac{n-1}{2}}$ is the volumetric rate of heat generation, and $K(x) = K_0(x+b)^{n-1}$ is a variable permeability.

The above system is completed with the following appropriate boundary conditions, taking to view of [32] and [33]:

$$u = U_w(x) = U_o(x+b)^n,\ v = 0,\ -k\frac{\partial T}{\partial y} = h_s(T_f - T),$$
$$D_B\frac{\partial C}{\partial y} + D_T\frac{\partial T}{\partial y} = 0 \text{ at } y = A(x+b)^{\frac{1-n}{2}}$$
$$u \longrightarrow 0, \quad T \longrightarrow T_\infty, \quad C \longrightarrow C_\infty \quad \text{as} \quad y \longrightarrow \infty \tag{5}$$

To the above equations, (1)-(4), the following relevant transformations will be utilized:

$$\psi = \sqrt{\frac{2}{n+1}\nu U_o(x+b)^{n+1}}f(\eta),$$
$$\xi = y\sqrt{(\frac{n+1}{2})\frac{U_o(x+b)^{n-1}}{\nu}}, \alpha = A\left(\frac{(n+1)U_0}{2\nu}\right)^{\frac{1}{2}}$$
$$\eta = \xi - \alpha = y\sqrt{(\frac{n+1}{2})\frac{U_o(x+b)^{n-1}}{\nu}} - \alpha$$
$$\theta = \frac{T - T_\infty}{T_w - T_\infty}, \quad \phi = \frac{C - C_\infty}{C_w - C_\infty}, \quad u = U_o(x+b)^n f'(\eta),$$
$$v = -\sqrt{\frac{2}{n+1}\nu U_o(x+b)^{n-1}}(f(\eta) + \eta\frac{n-1}{n+1}f'(\eta)). \tag{6}$$

Equation (1) is identically satisfied. In addition, when the above similarity variables are applied to Eqations (2), (3), and (4), it yields:

$$(\frac{\mu}{\mu_o}f'')' - \frac{2n}{n+1}f'^2 + ff'' + M(E_1 - f') - Kp\frac{\mu}{\mu_o}f' = 0, \tag{7}$$
$$(1 + \frac{4}{3}Rd)(\frac{k}{k_o}\theta')' + Pr_o(f\theta' + Nb\theta'\phi' + Nt(\theta')^2$$
$$+MEc(f' - E_1)^2 + \frac{2}{n+1}s\theta) = 0, \tag{8}$$

$$\phi'' + \frac{Nt}{Nb}\theta'' + LePr_o f\phi' = 0. \tag{9}$$

The equivalent boundary conditions in terms of similarity variables are specified as:

$$f(0) = \alpha(\frac{1-n}{1+n}),\ f'(0) = 1,\ ,f'(\infty) = 0,\ \theta'(0) = -B_i(1 - \theta(0))$$
$$\theta(\infty) = 0, \quad Nb\phi'(0) + Nt\theta'(0) = 0, \quad \phi(\infty) = 0, \tag{10}$$

where $M = \frac{2\sigma B_o^2}{\rho U_o(n+1)}$ is a magnetic parameter, α is the wall thickness parameter, $E_1 = \frac{E_o}{B_o U_o(x+b)^n}$ is the electric field, and

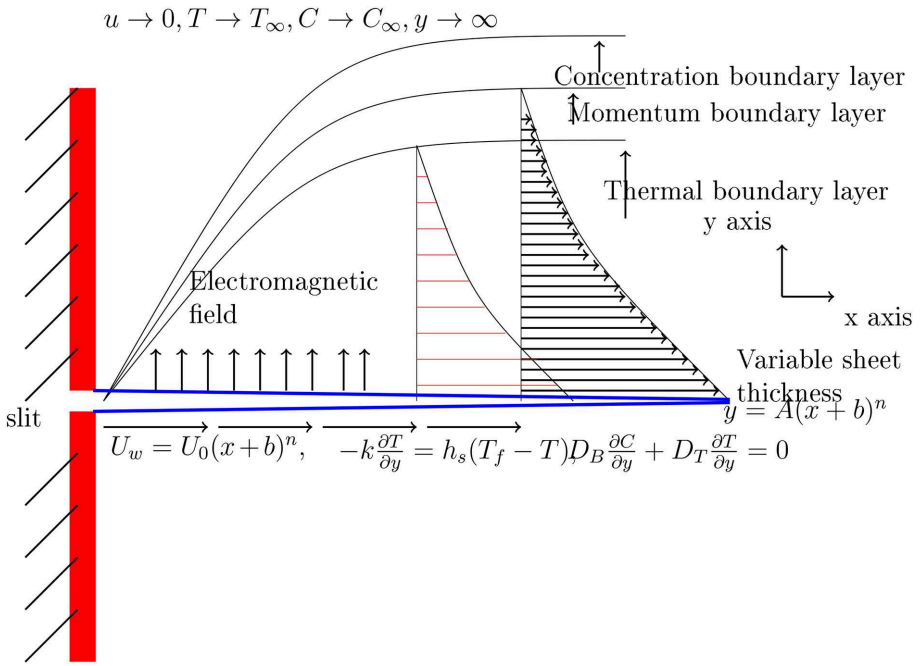

FIGURE 1 | Schematic diagram of the problem.

$Kp = \frac{2v}{K_o U_o(n+1)}$ is the permeability constant. $Pr_o = \frac{\mu_o C_p}{k_o}$ is the Prandtl number, $Nb = \frac{\tau D_B(C_w - C_\infty)}{v}$ is the Brownian motion parameter, $Nt = \frac{\tau D_T(T_w - T_\infty)}{T_\infty v}$ is the thermophoresis parameter, $Ec = \frac{U_w^2}{C_p(T_w - T_\infty)}$ is the local Eckert number, $Rd = \frac{4\sigma^* T_\infty^3}{k_o k^*}$ denotes the radiation parameter, $s = \frac{Q_o(x+b)}{\rho u_w C_p}$ is the heat source parameter, B_i is the Biot number, and $Le = \frac{v}{D_B}$ is Lewis number Irfan et al. [41].

3. FLUID PROPERTIES ANALYSIS

We illustrate the main theme of this work through the following two subsections.

3.1. Case A: Constant Fluid Characteristics

For this case, we rewrite Equations (7), (8), and (9) into the following set of equations Irfan et al. [41]:

$$f''' - \frac{2n}{n+1}f'^2 + ff'' + M(E_1 - f') - Kpf' = 0 \tag{11}$$

$$(1 + \frac{4}{3}Rd)\theta'' + Pr_o(f\theta' + Nb\theta'\phi' + Nt(\theta')^2 + MEc(f' - E_1)^2 + \frac{2}{n+1}s\theta) = 0 \tag{12}$$

$$\phi'' + \frac{Nt}{Nb}\theta'' + Pr_o Lef\phi' = 0 \tag{13}$$

3.2. Case B: Variable Fluid Properties

In this case, we express viscosity and thermal conductivity as a function of temperature Andersson and Aarseth [30]

$$\mu(T) = \frac{\mu_{ref}}{1 + \gamma(T - T_{ref})} \tag{14}$$

In (14), above, γ is a property of a fluid. Assuming $T_o \approx T_{ref}$, we get

$$\mu = \frac{\mu_o}{1 - \frac{T - T_o}{\theta_r(T_w - T_o)}} = \frac{\mu_o}{1 - \frac{\theta(\eta)}{\theta_r}} \tag{15}$$

Here, $\theta_r = \frac{-1}{\gamma(T_w - T_o)}$. Inserting Equation (15) into Equation (7), we get

$$\frac{\theta_r}{(\theta r - \theta)}f''' + \frac{f''\theta'\theta_r}{(\theta_r - \theta)^2} - \frac{2n}{n+1}f'^2 + ff'' + M(E_1 - f') - Kp\frac{\theta_r}{\theta_r - \theta}f' = 0 \tag{16}$$

Following Prasad et al. [31], the changeable thermal conductivity is expressed as

$$k(T) = k_o(1 + \epsilon\theta) \tag{17}$$

Using Equation (17) in Equation (8), we get.

$$(1 + \frac{4}{3}Rd)((1 + \epsilon\theta)\theta'' + \epsilon(\theta')^2) + Pr_o(f\theta' + Nb\theta'\phi' + Nt(\theta')^2 + MEc(f' - E_1)^2 + \frac{2}{n+1}s\theta) = 0 \tag{18}$$

4. PHYSICAL QUANTITIES

The important physical parameters are defined as follows.

4.1. Skin Friction Coefficient

The wall friction coefficients for case A and case B are defined as

$$C_f = \frac{\tau_w}{\rho u_w^2} = \sqrt{\frac{1+n}{2Re_x}} f''(0) \text{ (CASE A)}$$

$$C_f = \frac{\tau_w}{\rho u_w^2} = \frac{\theta_r}{\theta_r - \theta(0)} \sqrt{\frac{1+n}{2Re_x}} f''(0) \text{ (CASE B)}$$

4.2. Local Nusselt Number

The local Nusselt numbers for Cases A and B are the same and can be written as

$$Nu_x = -\frac{(x+b)q_w}{k_o(T_w - T_\infty)} = -(1 + \frac{4}{3}Rd)\sqrt{\frac{(1+n)Re_x}{2}}\theta'(0)$$

4.3. Local Sherwood Number

The local Sherwood number for both Case A and Case B is

$$Sh_x = -\frac{(x+b)j_w}{C_w - C_\infty} = -\sqrt{\frac{(1+n)Re_x}{2}}\phi'(0) \tag{19}$$

5. NUMERICAL PROCEDURE

The system of ODEs for Case A and Case B, along with the boundary conditions, are first transformed into a system of first-order ODEs. We use two numerical methods to find the solution of these ODEs. The first method is the SFDM [42], and the second is implemented through MATLAB's built-in solver *bvp4c*. The details of the methods and the implications are described below.

5.1. Simplified Finite Difference Method (SFDM)

The algorithm and necessary details for the simplified FDM are as follows:

1. We first reduce the third-order ODE into a group of first- and second-order ODEs. This reduction of order simplifies the process of finite difference approximation. The ODE already written in second order cannot be reduced.
2. For further simplification, we use a Taylor series to linearize the system of nonlinear ODEs.
3. We replace the derivatives in linear ODEs with the corresponding finite difference approximation formulas.
4. In the end, we reach an algebraic system of equations that can be solved efficiently by the Thomas algorithm.
5. The process will be repeated for energy and concentration equations.

An explanation of SFDM has been illustrated in the flowchart. Generally, we find the results when $N = 1,000$ grid points in the η direction. The domain to achieve steady state varies due to the effects of different parameters, but the domain $\eta = 7$ seems sufficient for our results. To initiate, we assume $f' = F$ in (11), and then we get

$$\frac{d^2F}{d\eta^2} = \frac{2n}{n+1}F^2 - f\frac{dF}{d\eta} - M(E_1 - F) + KpF \tag{20}$$

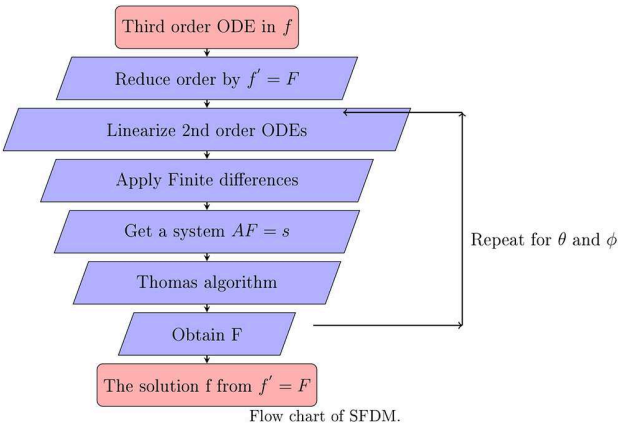

Flow chart of SFDM.

We can write this expression for the function f as

$$\chi_1(\eta, F, F') = \frac{2n}{n+1}F^2 - f\frac{dF}{d\eta} - M(E_1 - F) + KpF \tag{21}$$

Let us approximate $\frac{dF}{d\eta}$ in the above equation by forward difference approximation

$$\chi_1(\eta, F, F') = \frac{2n}{n+1}F_i^2 - f_i(\frac{F_{i+1} - F_i}{h}) - M(E_1 - F_i) + KpF_i \tag{22}$$

The coefficients of second-order ODE read as

$$A_n = -\frac{\partial \chi_1}{\partial F'} = -(-f) = f = f_i \tag{23}$$

$$B_n = -\frac{\partial \chi_1}{\partial F} = -(\frac{4n}{n+1}F + M + Kp) = -(\frac{4n}{n+1}F_i + M + Kp) \tag{24}$$

$$D_n = \chi_1(\eta, F, F') + B_nF_i + A_n\frac{F_{i+1} - F_i}{h} \tag{25}$$

After some manipulation, (25) becomes

$$a_iF_{i-1} + b_iF_i + c_iF_{i+1} = r_i, \qquad i = 1, 2, 3...., N \tag{26}$$

where

$$a_i = 2 - hA_n, \quad b_i = 2h^2B_n - 4, \quad c_i = 2 + hA_n, \quad r_i = 2h^2D_n \tag{27}$$

In matrix-vector form, it is written compactly as

$$AF = s \tag{28}$$

where

$$A = \begin{bmatrix} b_1 & c_1 & & & \\ a_2 & b_2 & c_2 & & \\ & .... & & & \\ & & a_{N-2} & b_{N-2} & c_{N-2} \\ & & & a_{N-1} & b_{N-1} \end{bmatrix} \tag{29}$$

$$F = \begin{bmatrix} F_1 \\ F_2 \\ . \\ . \\ F_{N-1} \end{bmatrix} \qquad s = \begin{bmatrix} s_1 \\ s_2 \\ . \\ . \\ s_{N-1} \end{bmatrix} \tag{30}$$

The matrix A is a tridiagonal matrix and is written in LU-Factorization as [43]

$$A = LU \tag{31}$$

where

$$L = \begin{bmatrix} \beta_1 & & & & \\ a_2 & \beta_2 & & & \\ & .... & & & \\ & & a_{N-2} & \beta_{N-2} & \\ & & & a_{N-1} & \beta_{N-1} \end{bmatrix} \tag{32}$$

and

$$U = \begin{bmatrix} 1 & \gamma_1 & & & \\ & 1 & \gamma_2 & & \\ & & .... & & \\ & & & 1 & \gamma_{N-2} \\ & & & & 1 \end{bmatrix} \tag{33}$$

where L and U are the lower and upper triangular matrices, respectively. Here the unknowns $(\beta_i, \gamma_i), i = 1, 2, ..., N-1$ are to be related as [43]

$$\beta_1 = -1 - \frac{\lambda}{h}, \quad \gamma_1 = \frac{\lambda}{\beta_1 h} \tag{34}$$

$$\beta_i = b_i - a_i\gamma_{i-1}, \quad i = 2, 3, ..., N-1 \tag{35}$$

$$\beta_i\gamma_i = c_i, \quad i = 2, 3, ..., N-2 \tag{36}$$

After defining these relations, (31) becomes

$$LUF = s, \qquad UF = z, \qquad \text{and} \quad Lz = s \tag{37}$$

and we have

$$\begin{bmatrix} \beta_1 & & & \\ a_2 & \beta_2 & & \\ & .... & & \\ & & a_{N-2} & \beta_{N-2} \\ & & & a_{N-1} \end{bmatrix} \begin{bmatrix} z_1 \\ z_2 \\ z_3 \\ . \\ . \\ . \\ z_{N-2} \\ z_{N-1} \end{bmatrix} = \begin{bmatrix} s_1 \\ s_2 \\ s_3 \\ . \\ . \\ . \\ s_{N-2} \\ s_{N-1} \end{bmatrix} \tag{38}$$

The unknown elements of z can be found by

$$z_1 = s_1/\beta_1, z_i = \frac{s_i - a_i z_{i-1}}{\beta_i}, i = 2, 3, ..., N-1 \tag{39}$$

and

$$\begin{bmatrix} 1 & \gamma_1 & & & \\ & 1 & \gamma_2 & & \\ & & .... & & \\ & & & 1 & \gamma_{N-2} \\ & & & & 1 \end{bmatrix} \begin{bmatrix} F_1 \\ F_2 \\ . \\ . \\ . \\ F_{N-2} \\ F_{N-1} \end{bmatrix} = \begin{bmatrix} z_1 \\ z_2 \\ . \\ . \\ . \\ z_{N-2} \\ z_{N-1} \end{bmatrix} \tag{40}$$

We then get

$$F_{i-1} = z_{i-1}, \qquad F_i = z_i - \gamma_i F_{i+1}, \qquad i = N-2, N-3, ..., 3, 2, 1 \tag{41}$$

which is a solution of (20). We can easily find f from $f^{'} = F$, which in discretization form

$$\frac{f_{i+1} - f_i}{h} = F_i \tag{42}$$

gives a required solution of (11). A similar procedure can also adopted for solutions θ and ϕ. For the sake of brevity, we only present coefficients for these ODEs and leave out the details that follow on the same line as presented above. For example, the energy equation (12) is

$$\frac{d^2\theta}{d\eta^2} = -(\frac{Pr_o}{(1+\frac{4}{3}Rd)}(f\frac{d\theta}{d\eta} + Nb\frac{d\theta}{d\eta}\frac{d\phi}{d\eta} + Nt(\frac{d\theta}{d\eta})^2 + MEc(\frac{df}{d\eta} - E_1)^2 + \frac{2}{n+1}s\theta)) \tag{43}$$

$$\chi_2(\eta, \theta, \theta^{'}) = -(\frac{Pr_o}{(1+\frac{4}{3}Rd)}(f_i(\frac{\theta_i - \theta_{i-1}}{h}) + Nb(\frac{\theta_i - \theta_{i-1}}{h})(\frac{\phi_i - \phi_{i-1}}{h}) + Nt(\frac{\theta_i - \theta_{i-1}}{h})^2 + MEc(F_i - E_1)^2 + \frac{2}{n+1}s\theta_i)) \tag{44}$$

$$A_{nn} = -\frac{\partial\chi}{\partial\theta^{'}} = -(-\frac{Pr_o}{(1+\frac{4}{3}Rd)}(f + Nb\phi^{'} + (2Nt\theta^{'}) \tag{45}$$

$$A_{nn} = \frac{Pr_o}{(1+\frac{4}{3}Rd)}(f_i + Nb(\frac{\phi_i - \phi_{i-1}}{h}) + 2N_t(\frac{\theta_i - \theta_{i-1}}{h})) \tag{46}$$

$$B_{nn} = \frac{2Pr_o}{(n+1)(1+4/3Rd)}s \tag{47}$$

$$\frac{d^2\phi}{d\eta^2} = \frac{-Nt}{Nb}\frac{d^2\theta}{d\eta^2} - LePr_o f\phi^{'} \tag{48}$$

$$\chi_3(\eta, \phi, \phi^{'}) = \frac{-Nt}{Nb}\frac{\theta_{i-1} - 2\theta_i + \theta_{i+1}}{h^2} - LePr_o(f_i\frac{\phi_i - \phi_{i-1}}{h}) \tag{49}$$

Similarly, the coefficients for (13) are written as

$$A_{nnn} = Pr_o Le f_i, \qquad B_{nnn} = 0 \tag{50}$$

Boundary conditions can easily be discretized by following the above procedure.

5.2. bvp4c

To solve the system of ODEs for Case A and Case B, we first transformed the system into first-order ODEs to compute the solution using *bvp4c*. For Case A it gives,

(a) Case A:

$$f = v_1, f' = v_2, f'' = v_3, f''' = v_3' = \frac{2n}{n+1}v_2^2 - v_1 v_3 - M(E_1 - v_2) + Kpv_2,$$

TABLE 1 | Resemblance of $-f''(0)$ from the literature for various n values (**CASE A**).

n	α	Fang et al. [4]	Khader and Ahmed [5]	Present result (bvp4c)	Present result (SFDM)
10	0.25	1.1433	1.1433	1.1433	1.1433
9		1.1404	1.1404	1.1404	1.1404
7		1.1323	1.1322	1.1323	1.1323
5		1.1186	1.1186	1.1186	1.1186
3		1.0905	1.0904	1.0905	1.0905
1		1.0000	1.0000	1.0000	1.0000
0.5		0.9338	0.9337	0.9338	0.9338
0		0.7843	0.7843	0.7843	0.7843
−1/3		0.5000	0.5000	0.5000	0.5025
−0.5		0.0833	0.0833	0.0833	0.0867
10	0.5	1.0603	1.0603	1.0603	1.0603
9		1.0589	1.0588	1.0589	1.0589
7		1.0550	1.0551	1.0551	1.0551
5		1.0486	1.0486	1.0486	1.0486
3		1.0359	1.0358	1.0359	1.0359
2		1.0234	1.0234	1.0234	1.0234
1		1.0000	1.0000	1.0000	1.0000
0.5		0.9799	0.9798	0.9799	0.9798
0.00		0.9576	0.9577	0.9576	0.9577
−0.5		1.1667	1.1667	1.1667	1.1669

TABLE 2 | Resemblance of the values of $-f''(0)$ for different values of parameters M, n, α, E_1, and θ_r.

						Case B		Case A	
M	n	α	E_1	Kp	θ_r	$-f''(0)$(*bvp4c*)	$-f''(0)$ (SFDM)	$-f''(0)$(*bvp4c*)	$-f''(0)$ (SFDM)
0	0.5	0.3	0.1	0.1	−5	1.075408	1.075408	0.996308	0.996308
0.3						1.184031	1.184031	1.097247	1.097247
0.7						1.335487	1.335487	1.236298	1.236298
0.1	0					0.983771	0.987475	0.907889	0.907889
	0.5					1.106245	1.106245	1.025923	1.025923
	1					1.160763	1.160763	1.078835	1.078835
	0.5	0.4				1.125682	1.125682	1.043448	1.043448
		0.7				1.185376	1.185376	1.097515	1.097515
		1				1.247097	1.247097	1.153791	1.153791
		0.3	0.5			1.025633	1.025633	0.954581	0.954581
			1			0.940761	0.940761	0.877466	0.877466
			1.5			0.864007	0.864007	0.807036	0.807036
			0.1	0.1		1.106245	1.106245	1.025923	1.025923
				0.3		1.205899	1.205899	1.12657	1.12657
				0.5		1.294325	1.294325	1.216757	1.216757
				0.1	−10	1.066455	1.066455		
					−1	1.391356	1.391356		
					−0.5	1.703479	1.703479		

TABLE 3 | Comparison of the values of $-\theta^{'}(0)$ and $\phi^{'}(0)$ for different values of *Rd*, *Ec*, *Le*, *Nb*, *Nt*, *n*, Pr_o, *s*, α, and ϵ for Case B with Case A, respectively.

										Case B		Case A	
Rd	***Ec***	***Le***	***Nb***	***Nt***	***n***	***Pr_o***	***s***	***α***	***ϵ***	***$-\theta^{'}(0)$***	***$-\phi^{'}(0)$***	***$-\theta^{'}(0)$***	***$-\phi^{'}(0)$***
0.4	0.1	1	0.1	0.2	0.5	1	0.1	0.3	0.2	0.2125241	−0.4250431	0.2477734	−0.4955469
0.7										0.1682977	−0.3365954	0.2047175	−0.409435
1										0.1331988	−0.2663976	0.1704	−0.3407401
0.2	0.2									0.2450324	−0.4900648	0.2790463	−0.5580926
	0.6									0.2263721	−0.4527441	0.2603162	−0.5206325
	1									0.2077006	−0.4154012	0.2415691	−0.4831381
	0.1	0.7								0.2507037	−0.5014074	0.2847274	−0.5694548
		1								0.2496957	−0.4993915	0.2837261	−0.5674523
		1.3								0.2489893	−0.4979786	0.283001	−0.566002
		1	0.2							0.2496958	−0.2496958	0.2837261	−0.2837261
			0.5							0.2496958	−0.0998783	0.2837261	−0.1134905
			0.7							0.2496958	−0.07134165	0.2837261	−0.08106461
			0.1	0.1						0.2532452	−0.2532452	0.2869886	−0.2869886
				0.2						0.249657	−0.4993915	0.2837261	−0.5674523
				0.4						0.2424194	−0.969777	0.2770397	−1.108159
				0.2	0					0.28097	−0.5619401	0.3176236	−0.6352471
					0.5					0.2496957	−0.4993915	0.2837261	−0.5674523
					1					0.236645	−0.4732899	0.268578	−0.5371561
					0.5	0.7				0.1808165	−0.361633	0.2169344	−0.4338689
						1				0.2496957	−0.4993915	0.2837261	−0.5674523
						1.3				0.3014584	−0.6029168	0.3334471	−0.6668941
						1	0			0.3226349	−0.6452698	0.3492327	−0.6984654
							0.1			0.2496957	−0.4993915	0.2837261	−0.5674523
							0.1	0.4		0.2597021	−0.5194042	0.2935494	−0.5870988
								0.7		0.2886493	−0.5772986	0.3219052	−0.6438104
								1		0.3160671	−0.6321342	0.3486554	−0.6973109
								0.3	0.3	0.2380814	−0.4761629		
									0.5	0.2168179	−0.4336357		
									0.8	0.1892523	−0.3785047		

$$v_4 = \theta, v_5 = \theta^{'}, \theta^{''} = v_5^{'} = -\frac{Pr_o}{(1+\frac{4}{3})Rd}(v_1 v_5 + Nb v_5 v_7 + Nt v_5^2 + MEc(v_2 - E_1)^2 + \frac{2}{n+1} s v_4),$$

$$v_6 = \phi, v_7 = \phi^{'}, \phi^{''} = v_7^{'} = -LePr_o v_1 v_7 - \frac{Nt}{Nb} v_5^{'}.$$

(b) Case B: The transformed ODEs for Case B are,

$$f = u_1, f^{'} = u_2, f^{''} = u_3, f^{'''} = u_3^{'} = \frac{(u_3 u_5)}{(u_4 - \theta_r)} + \frac{(u_4 - \theta_r)}{\theta_r}(-\frac{2n}{n+1} u_2^2 + u_1 u_3 + M(E_1 - u_2) - Kp u_2),$$

$$u_4 = \theta, u_5 = \theta^{'}, \theta^{''} = u_5^{'} = \frac{-\epsilon u_5^2}{1+\epsilon u_4} - \frac{Pr_o}{(1+\epsilon u_4)(1+\frac{4}{3}Rd)}(u_1 u_5 + Nb u_5 u_7 + Nt u_5^2 + MEc(u_2 - E_1)^2 + \frac{2}{n+1} s u_4),$$

$$u_6 = \phi, u_7 = \phi^{'}, \phi^{''} = u_7^{'} = -LePr_o u_1 u_7 - \frac{Nt}{Nb} u_5^{'}.$$

6. RESULT AND DISCUSSION

In this section, we present the outcomes of our results both in tabulated and graphical forms.

In **Table 1**, we compare our results with the literature for the skin friction coefficient against different values of *n* while fixing $\alpha = 0.25$ and $\alpha = 0.5$. The SFDM shows an excellent agreement with *bvp4c* and the literature. In summary, the skin friction coefficient is higher for Case B and lower values for Case A.

In **Table 2** we calculate the skin friction coefficient for various parameters like magnetic parameter *M*, power law index *n*, electric field E_1, porosity parameter *Kp*, variable thickness α, and viscosity parameter θ_r. Its value goes up by changing *M*, *n*, α, *Kp*, and θ_r, while it gets lower by changing E_1. **Table 3** shows the heat and mass transfer rates for various parameters.

An electric field parameter, E_1, enhances the velocity of the fluid, as can be seen in **Figure 2**. Lorentz force is responsible for increasing velocity due to the fact that the skin friction coefficient (as shown in **Table 2**) decreases.

In **Figure 3**, we observe that the momentum boundary layer thickness thins with an increase in porosity parameter *Kp*. This decrease in velocity profile is due to an increase in skin friction for increasing values of porosity parameter *Kp*. Moreover, increasing

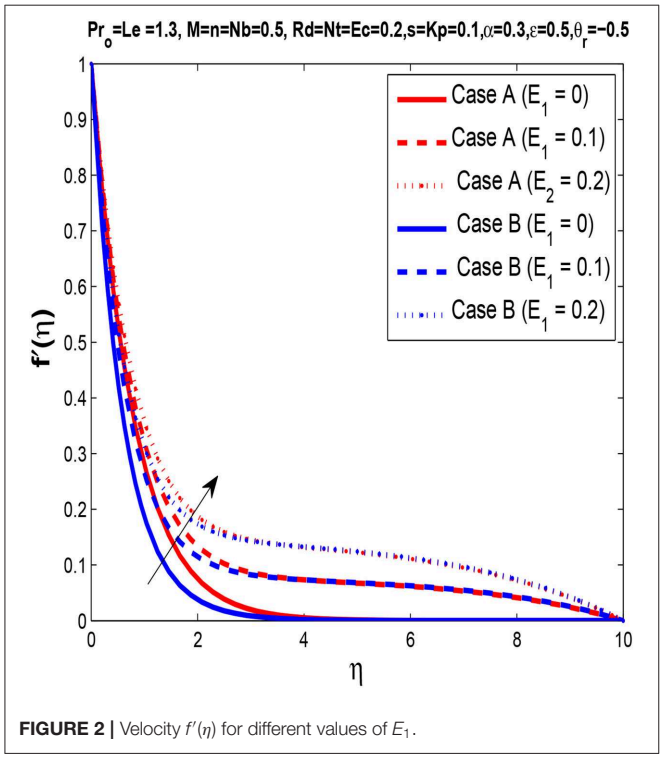

FIGURE 2 | Velocity $f'(\eta)$ for different values of E_1.

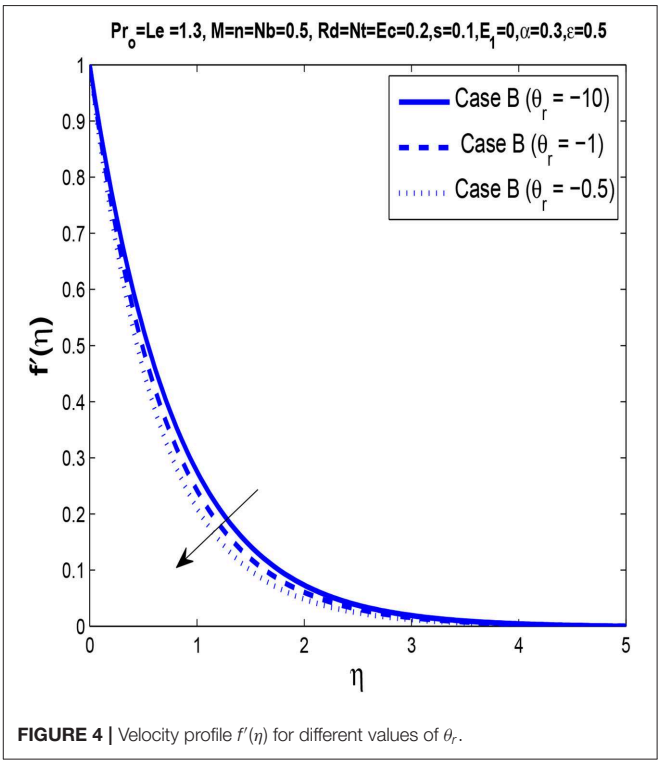

FIGURE 4 | Velocity profile $f'(\eta)$ for different values of θ_r.

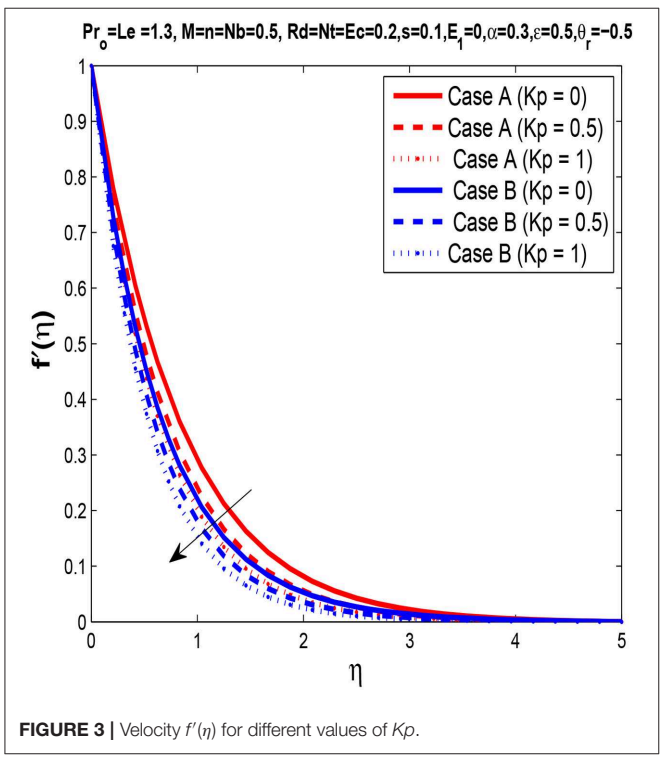

FIGURE 3 | Velocity $f'(\eta)$ for different values of *Kp*.

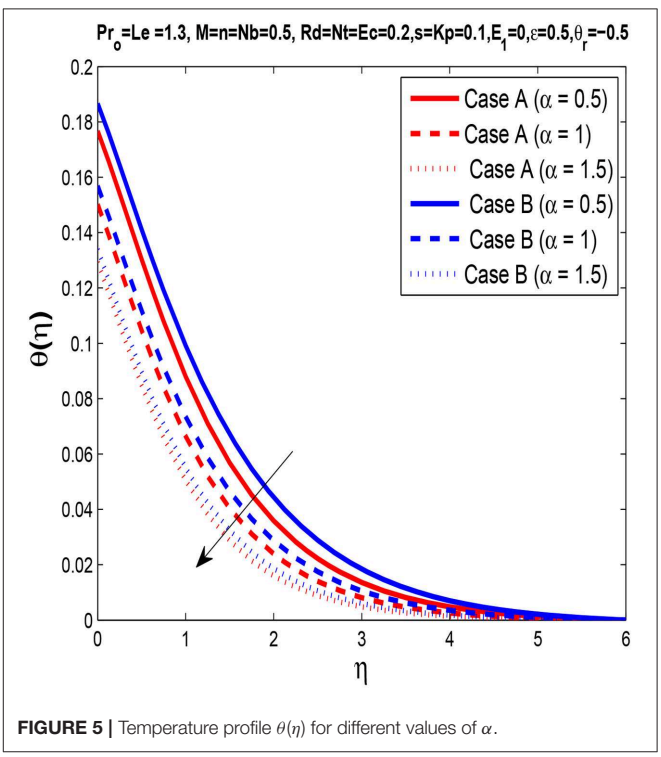

FIGURE 5 | Temperature profile $\theta(\eta)$ for different values of α.

porosity provides resistance to the flow, which ultimately reduces the velocity of the fluid.

Figure 4 describes the velocity profile for different values of viscosity parameter θ_r. It is observed that the momentum boundary layer thins with an increase in fluid viscosity parameter θ_r. This can be related to **Table 2**, where we can see that increasing viscosity parameter θ_r leads to the magnitude of the skin friction coefficient increasing, which causes the reduction in velocity. Increasing viscosity provides more resistance to the fluid motion since higher shear stress is required to move viscous fluids.

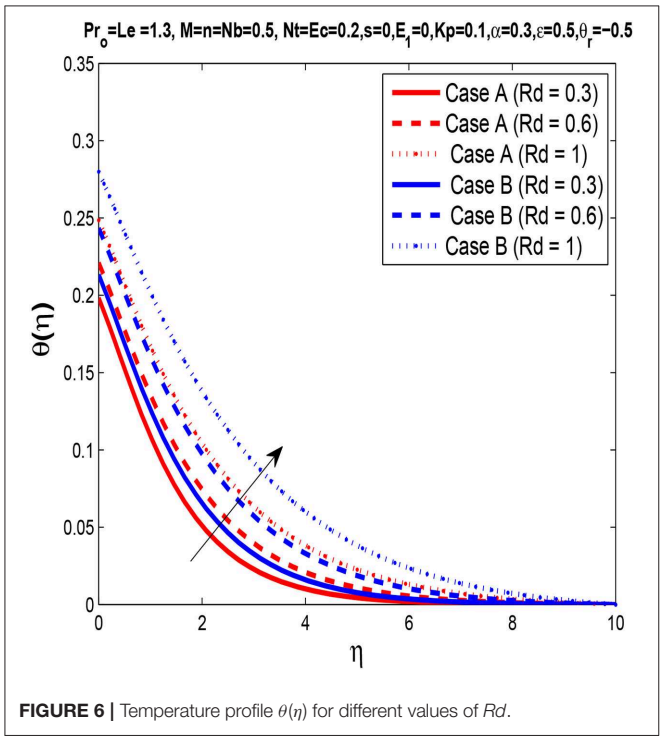

FIGURE 6 | Temperature profile $\theta(\eta)$ for different values of *Rd*.

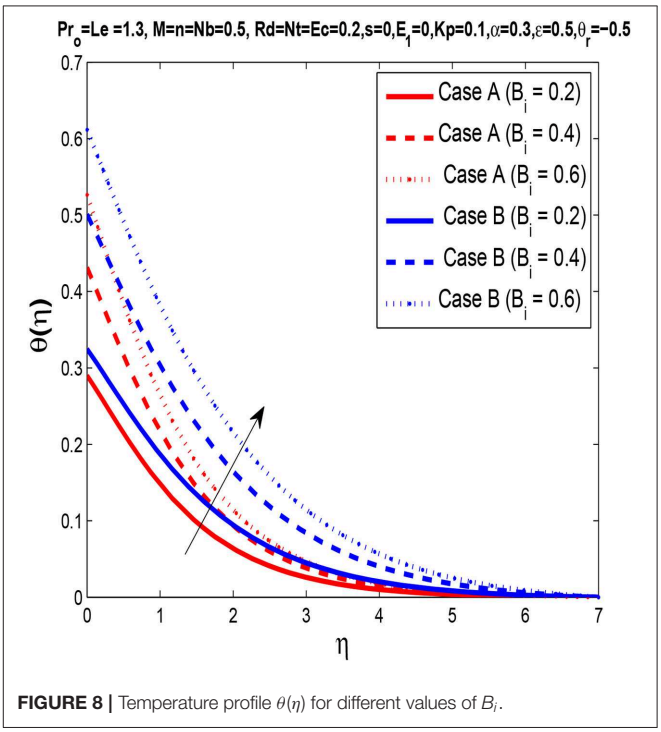

FIGURE 8 | Temperature profile $\theta(\eta)$ for different values of B_i.

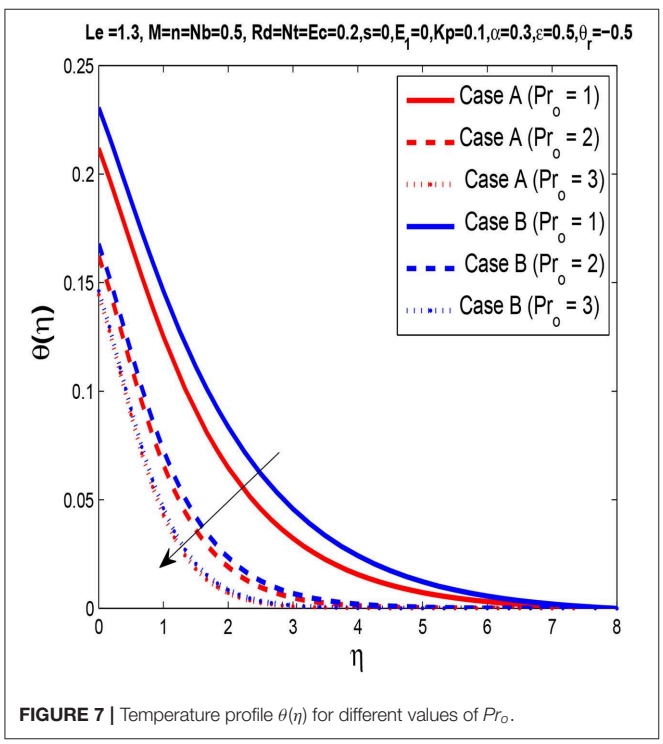

FIGURE 7 | Temperature profile $\theta(\eta)$ for different values of Pr_o.

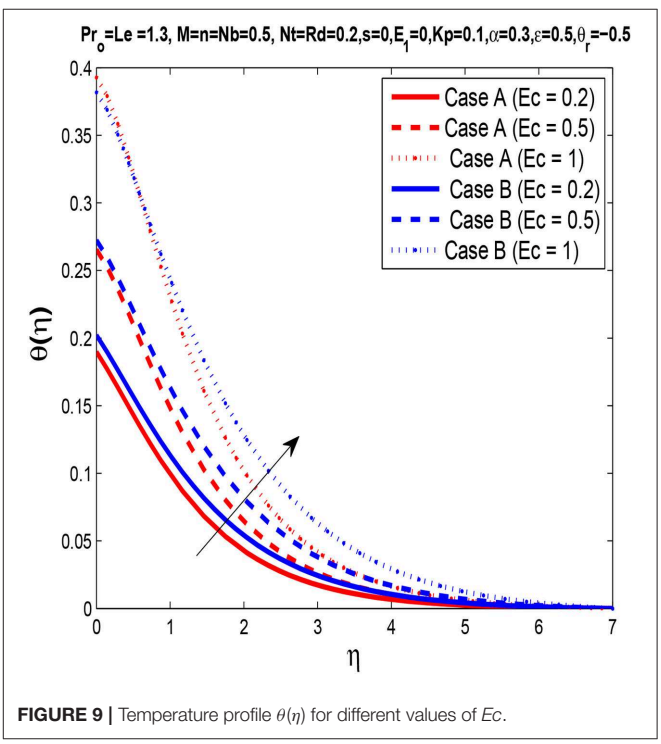

FIGURE 9 | Temperature profile $\theta(\eta)$ for different values of *Ec*.

The effect of variable thickness parameter α on temperature can be seen in **Figure 5**. It is observed that only some energy is transmitted from the surface to the liquid when we raise the wall thickness parameter. Physically, it shows that as we enhance wall thickness parameter α, less heat is transferred from the sheet to the fluid. The temperature profile therefore decreases.

Figure 6 is plotted to demonstrate the effect of thermal radiation parameter *Rd* on the temperature profile. It is found that with the rise in *Rd*, the temperature profile increases significantly, as an increase in the radiation parameter provides more energy to the fluid, which increases the thickness of the thermal boundary layer.

In **Figure 7**, it is observed that an increase in Prandtl number Pr_o causes a reduction in the temperature profile. The reason for this decrease is that smaller values of Prandtl number Pr_0 are equivalent higher thermal conductivity. Since the thermal conductivity of air is higher, ultimately, the temperature is higher. However, a high Prandtl number corresponds to low thermal conductivity and lower temperature flow.

In **Figure 8**, we illustrate the influence of Biot number B_i on the temperature profile. It is seen that for higher values of Biot number B_i, the thermal boundary layer thickness increases. This increase in temperature profile is due to the heat transfer rate, which enhances for higher values of Biot number B_i. Since the thermal conductivity is dominant compared to convection, heat transport increases as the Biot number increases.

To examine the effects of the Eckert number *Ec* on the temperature distribution, we plot **Figure 9**. For higher values of the Eckert number *Ec*, it is evaluated that somehow the temperature profile rises and the thermal boundary layer gets thinner. Eckert number *Ec* is the ratio of the kinetic energy of fluid and enthalpy. For increasing values of Eckert number *Ec*, the kinetic energy increases, which causes an enhancement in fluid temperature.

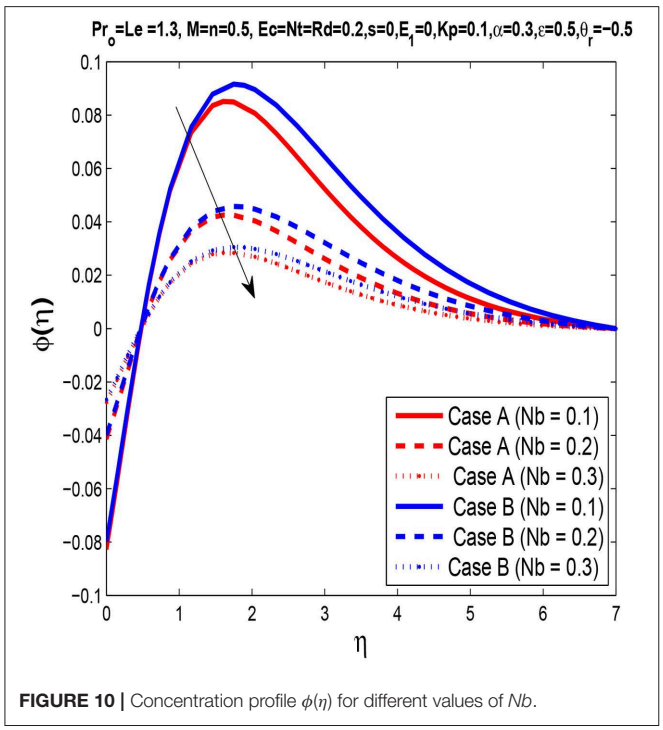

FIGURE 10 | Concentration profile $\phi(\eta)$ for different values of *Nb*.

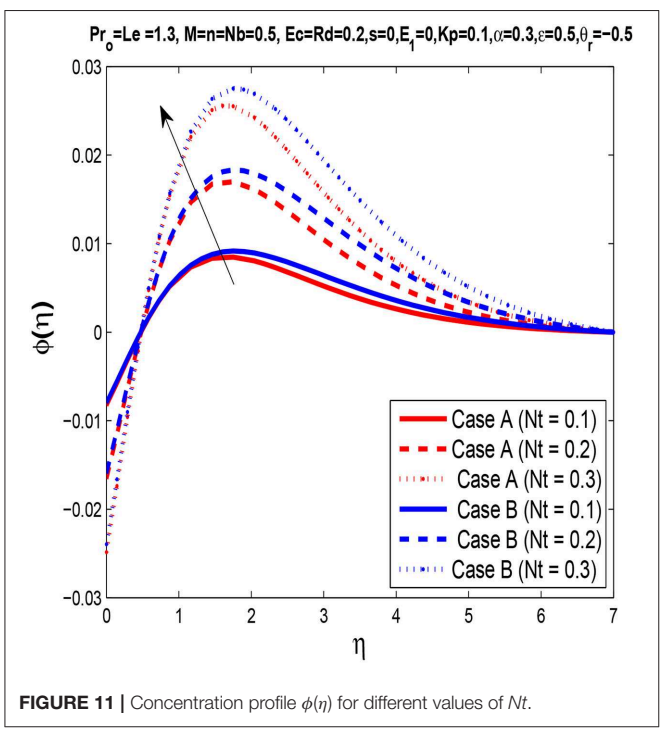

FIGURE 11 | Concentration profile $\phi(\eta)$ for different values of *Nt*.

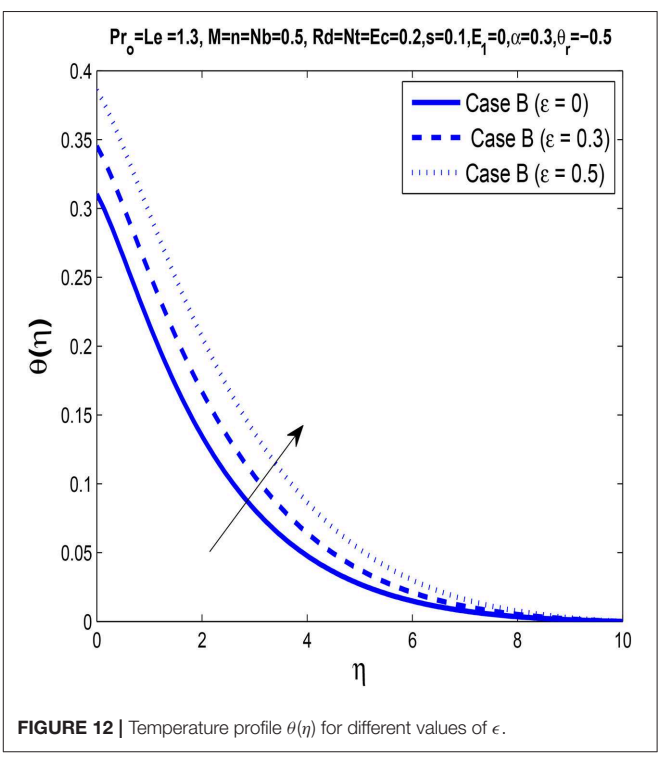

FIGURE 12 | Temperature profile $\theta(\eta)$ for different values of ϵ.

Figure 10 is plotted to illustrate the effect of the Brownian motion parameter on the concentration profile. It is concluded that higher values of Brownian motion parameter Nb cause a reduction in the nanoparticle concentration profile.

Figure 11 is presented to characterize the behavior of thermophoresis parameter Nt on the concentration profile. It is noted that by increasing the thermophoresis parameter, we find a reduction in the nanoparticle concentration profile.

In **Figure 12**, it is found that an increase in variable thermal conductivity parameter ϵ enhances the temperature profile. **Table 3** indicates that the Nusselt number decreases with increasing ϵ. Due to this, the heat transfer rate increases, and hence the temperature profile increases.

7. CONCLUSIONS

This analysis achieved two goals. Firstly, an assessment of distinctive features for constant and variable properties has been done. Secondly, we adopted a new numerical process, the SFDM, to compute solutions and compared its accuracy with *bvp4c*. The notable results for both cases, Case A and B, are as follows:

- The numerical technique, the SFDM, has produced excellent results with high accuracy, as shown in **Tables 1**, **2**.
- Momentum boundary layer thickness grows with an increase in the electric field E_1, whereas it decreases with increases in porosity parameter Kp and fluid viscosity parameter θ_r.
- The thermal boundary layer thickness rises when radiation parameter Rd, Biot number B_i, Eckert number Ec, or thermal conductivity parameter ϵ rises, while it decreases for higher values of variable thickness parameter α and Prandtl number Pr_o.
- The concentration boundary layer thickness decreases with increasing Nb and increases with increasing Nt.
- It is shown that the results are different for constant and variable fluid properties. For variable fluid properties, heat transfer and mass transfer rates are lower than with constant fluid properties. The skin friction coefficient is higher for variable fluid properties than for constant fluid properties.

AUTHOR CONTRIBUTIONS

MI and MF have jointly written the manuscript. The numerical part of bvp4c, as well as tables and graphs, have been completed by MI. TI investigated the SFDM for comparison. MF, MI, and TI have discussed results.

ACKNOWLEDGMENTS

MF would like to thank Research Scientist S. Hussain for his valuable contributions in the numerical part of this work.

REFERENCES

1. Hayat T, Ijaz Khan M, Farooq M, Alsaedi A, Waqas M, Yasmeen T. Impact of Cattaneo–Christov heat flux model in flow of variable thermal conductivity fluid over a variable thicked surface. *Int J Heat Mass Transfer.* (2016) 99:702–10. doi: 10.1016/j.ijheatmasstransfer.2016.04.016
2. Hayat T, Farooq M, Alsaedi A, Falleh Al-Solamy. Impact of Cattaneo-Christov heat flux in the flow over a stretching sheet with variable thickness. *AIP Adv.* (2015) 5:087159. doi: 10.1063/1.4929523
3. Mabood F, Ibrahim SM, Rashidi MM, Shadloo MS, Lorenzini G. Non-uniform heat source/sink and Soret effects on MHD non-Darcian convective flow past a stretching sheet in a micropolar fluid with radiation. *Int J Heat Mass Transfer.* (2016) 93:674–82. doi: 10.1016/j.ijheatmasstransfer.2015.10.014
4. Fang T, Zhang J, Zhong Y. Boundary layer flow over a stretching sheet with variable thickness. *Appl Math Comput.* (2012) 218:7241–52. doi: 10.1016/j.amc.2011.12.094
5. Khader MM, Megahed AM. Numerical solution for boundary layer flow due to a nonlinearly stretching sheet with variable thickness and slip velocity. *Eur Phys J Plus.* (2013) 128:100. doi: 10.1140/epjp/i2013-13100-7
6. Daniel YS, Abdul Aziz Z, Ismail Z, Salah F. Thermal stratification effects on MHD radiative flow of nanofluid over nonlinear stretching sheet with variable thickness. *J Comput Design Eng.* (2018) 5:232–42. doi: 10.1016/j.jcde.2017.09.001
7. Reddy S, Naikoti K, Rashidi MM. MHD flow and heat transfer characteristics of Williamson nanofluid over a stretching sheet with variable thickness and variable thermal conductivity. *Trans A Razmadze Math Inst.* (2017) 171:195–211. doi: 10.1016/j.trmi.2017.02.004
8. Daniel YS, Aziz ZA, Ismail Z, Salah F. Impact of thermal radiation on electrical MHD flow of nanofluid over nonlinear stretching sheet with variable thickness. *Alexandria Eng J.* (2018) 57:2187–97. doi: 10.1016/j.aej.2017.07.007
9. Akbar NS, Nadeem S, Ul Haq R, Khan ZH. Numerical solutions of Magnetohydrodynamic boundary layer flow of tangent hyperbolic fluid towards a stretching sheet. *Indian J Phys.* (2013) 87:1121–4. doi: 10.1007/s12648-013-0339-8
10. Mukhopadhyay S, Layek GC, Samad SA. Study of MHD boundary layer flow over a heated stretching sheet with variable viscosity. *Int J Heat Mass Transfer.* (2005) 48:4460–6. doi: 10.1016/j.ijheatmasstransfer.2005.05.027
11. Nadeem S, Ul Haq R, Akbar NS, Khan ZH. MHD three-dimensional Casson fluid flow past a porous linearly stretching sheet. *Alexandria Eng J.* (2013) 52:577–82. doi: 10.1016/j.aej.2013.08.005
12. Mabood F, Khan WA, Ismail AM. MHD boundary layer flow and heat transfer of nanofluids over a nonlinear stretching sheet: a numerical study. *J Magnet Magnet Mater.* (2015) 374:569–76. doi: 10.1016/j.jmmm.2014.09.013
13. Zhang C, Zheng L, Zhang X, Chen G. MHD flow and radiation heat transfer of nanofluids in porous media with variable surface heat flux and chemical reaction. *Appl Math Modell.* (2015) 39:165–81. doi: 10.1016/j.apm.2014.05.023
14. Poply V, Singh P, Yadav AK. A study of temperature-dependent fluid properties on MHD free stream flow and heat transfer over a non-linearly stretching sheet. *Proc Eng.* (2015) 127:391–7. doi: 10.1016/j.proeng.2015.11.386
15. Sheikholeslami M, Bandpy MG, Ellahi R, Zeeshan A. Simulation of MHD CuO-water nanofluid flow and convective heat transfer considering Lorentz forces. *J Magnet Magnet Mater.* (2014) 369:69–80. doi: 10.1016/j.jmmm.2014.06.017
16. Patel HR. Effects of heat generation, thermal radiation, and hall current on MHD Casson fluid flow past an oscillating plate in porous medium. *Multiphase Sci Technol.* (2019) 31:87–107. doi: 10.1615/MultScienTechn.2019029514
17. Farooq U, Lu D, Munir S, Ramzan M, Suleman M, Hussain S. MHD flow of Maxwell fluid with nanomaterials due to an exponentially stretching surface. *Sci Rep.* (2019) 9:7312. doi: 10.1038/s41598-019-43549-0
18. Ibrahim W, Tulu A. Magnetohydrodynamic (MHD) boundary layer flow past a wedge with heat transfer and viscous effects of nanofluid embedded in porous media. *Math Problems Eng.* (2019) 2019:4507852. doi: 10.1155/2019/4507852

19. Ali A, Shehzadi K, Sulaiman M, Asghar S. Heat and mass transfer analysis of 3D Maxwell nanofluid over an exponentially stretching surface. *Phys Script.* (2019) 94:065206. doi: 10.1088/1402-4896/ab07cf
20. Choi SUS, Eastman JA. *Enhancing Thermal Conductivity of Fluids With Nanoparticles.* Argonne National Lab., IL (1995).
21. Das K, Duari PR, Kundu PK. Numerical simulation of nanofluid flow with convective boundary condition. *J Egypt Math Soc.* (2015) 23:435–39. doi: 10.1016/j.joems.2014.05.009
22. Mabood F, Das K. Melting heat transfer on hydromagnetic flow of a nanofluid over a stretching sheet with radiation and second-order slip. *Eur Phys J Plus.* (2016) 131:3. doi: 10.1140/epjp/i2016-16003-1
23. Cao Z, Zhao J, Wang Z, Liu F, Zheng L. MHD flow and heat transfer of fractional Maxwell viscoelastic nanofluid over a moving plate. *J Mol Liquids.* (2016) 222:1121–7. doi: 10.1016/j.molliq.2016.08.012
24. Das K, Duari PR, Kundu PK. Effects of magnetic field on an unsteady mixed convection flow of nanofluids containing spherical and cylindrical nanoparticles. *J Heat Transfer.* (2016) 138:061901. doi: 10.1115/1.4032835
25. Satya Narayana PV, Venkateswarlu B, Venkataramana S. Thermal radiation and heat source effects on a MHD nanofluid past a vertical plate in a rotating system with porous medium. *Heat Transfer Asian Res.* (2015) 44:1–19. doi: 10.1002/htj.21101
26. Mansur S, Ishak A, Pop I. Stagnation-point flow towards a stretching/shrinking sheet in a nanofluid using Buongiorno's model. *Proc Inst Mech Eng : J Process Mech Eng.* (2017) 231:172–80. doi: 10.1177/0954408915585047
27. Makinde OD. Effects of viscous dissipation and Newtonian heating on boundary-layer flow of nanofluids over a flat plate. *Int J Num Methods Heat Fluid Flow.* (2013) 23:1291–303. doi: 10.1108/HFF-12-2011-0258
28. Ali AO, Makinde OD, Nkansah-Gyekye Y. Numerical study of unsteady MHD Couette flow and heat transfer of nanofluids in a rotating system with convective cooling. *Int J Num Methods Heat Fluid Flow.* (2016) 26:1567–79. doi: 10.1108/HFF-10-2014-0316
29. Ashwinkumar GP, Sulochana C. Effect of radiation absorption and buoyancy force on the MHD mixed convection flow of Casson nanofluid embedded with Al50Cu50 alloy nanoparticles. *Multidiscipl Model Mater Struct.* (2018) 14:1082–100. doi: 10.1108/MMMS-12-2017-0164
30. Andersson HI, Aarseth JB. Sakiadis flow with variable fluid properties revisited. *Int J Eng Sci.* (2007) 45:554–61. doi: 10.1016/j.ijengsci.2007.04.012
31. Prasad KV, Vajravelu K, Datti PS. The effects of variable fluid properties on the hydro-magnetic flow and heat transfer over a non-linearly stretching sheet. *Int J Thermal Sci.* (2010) 49:603–10. doi: 10.1016/j.ijthermalsci.2009.08.005
32. Hayat T, Shehzad SA, Qasim M, Alsaedi A. Mixed convection flow by a porous sheet with variable thermal conductivity and convective boundary condition. *Braz J Chem. Eng.* (2014) 31:109–17. doi: 10.1590/S0104-66322014000100011
33. Bhaskar Reddy N, Poornima T, Sreenivasulu P. Influence of variable thermal conductivity on MHD boundary layer slip flow of ethylene-glycol based Cu nanofluids over a stretching sheet with convective boundary condition. *Int J Eng Math.* (2014) 2014:905158. doi: 10.1155/2014/905158
34. Ullah MZ, Serra-Capizzano S, Baleanu D. A numerical simulation for Darcy-Forchheimer flow of nanofluid by a rotating disk with partial slip effects. *Front Phys.* (2019) 7:219. doi: 10.3389/fphy.2019.00219
35. Shah Z, Babazadeh H, Kumam P, Shafee A, Thounthong P. Numerical simulation of magnetohydrodynamic nanofluids under the influence of shape factor and thermal transport in a porous media using CVFEM. *Front Phys.* (2019) 7:164. doi: 10.3389/fphy.2019.00164
36. Zeeshan A, Shehzad N, Abbas T, Ellahi R. Effects of radiative electro-magnetohydrodynamics diminishing internal energy of pressure-driven flow of titanium dioxide-water nanofluid due to entropy generation. *Entropy.* (2019) 21:236. doi: 10.3390/e21030236
37. Ellahi R, Sait SM, Shehzad N, Mobin N. Numerical simulation and mathematical modeling of electro-osmotic Couette-Poiseuille flow of MHD power-law nanofluid with entropy generation. *Symmetry.* (2019) 11:1038. doi: 10.3390/sym11081038
38. Yousif MA, Ismael HF, Abbas T, Ellahi R. Numerical study of momentum and heat transfer of MHD Carreau nanofluid over an exponentially stretched plate with internal heat source/sink and radiation. *Heat Transfer Res.* (2019) 50:649–58. doi: 10.1615/HeatTransRes.2018025568
39. Sarafraz MM, Pourmehran O, Yang B, Arjomandi M, Ellahi R. Pool boiling heat transfer characteristics of iron oxide nano-suspension under constant magnetic field. *Int J Thermal Sci.* (2020) 147:106131. doi: 10.1016/j.ijthermalsci.2019.106131
40. Fujimoto K. Multi-scale kinetic simulation of magnetic reconnection with dynamically adaptive meshes. *Front Phys.* (2018) 6:119. doi: 10.3389/fphy.2018.00119
41. Irfan M, Farooq MA. Magnetohydrodynamic free stream and heat transfer of nanofluid flow over an exponentially radiating stretching sheet with variable fluid properties. *Front Phys.* (2019) 7:186. doi: 10.3389/fphy.2019.00186
42. Na TY, editor. *Computational Methods in Engineering Boundary Value Problems.* Academic Press (1980).
43. Thomas LH. *Elliptic Problems in Linear Difference Equations Over a Network.* New York, NY: Watson Sci. Comput. Lab. Rept., Columbia University (1949).

Conflict of Interest: The authors declare that the research was conducted in the absence of any commercial or financial relationships that could be construed as a potential conflict of interest.

NOMENCLATURE

(u, v)	Velocity components
b	Positive constant
n	Power law index
$B(x)$	Applied magnetic field
$E(x)$	Applied electric field
μ	Coefficient of viscosity
ρ	Density of fluid
σ	Electrical conductivity of the fluid
M	Magnetic field parameter
E_1	Electric field parameter
Kp	Permeability parameter
T	Fluid temperature
k	Thermal conductivity
C_p	Specific heat capacity
q_r	Radiative heat flux
$Q(x)$	Heat generation/absorption parameter
C	Concentration
τ	Ratio of heat capacities of nanofluid to heat capacities of base fluid
$(\rho C)_p$	Heat capacities of nanofluid
$(\rho C)_f$	Heat capacities of base fluid
D_B	Brownian coefficients
D_T	Thermophoretic diffusion coefficients
T_∞	Ambient fluid temperature
T_w	Constant temperature at wall
C_∞	Ambient fluid concentration
C_w	Fluid concentration at wall
Pr_o	Prandtl number
Le	Lewis number
Nt	Thermophoresis number
Nb	Brownian motion parameter
α	Wall thickness parameter
Rd	Thermal radiation parameter
σ^*	Stefan-Boltzman constant
k^*	Mean absorption coefficient
ϵ	Thermal conductivity parameter of the fluid
θ_r	Fluid viscosity parameter
B_i	Biot number
Ec	Eckert number
s	Heat source parameter
Re_x	Local Reynolds number
τ_w	Surface shear stress
q_w	Wall heat flux
j_w	Wall mass flux
$C_f = \frac{\tau_w}{\frac{\rho u_w^2}{2}}$	Skin friction coefficient
$Nu_x = -\frac{(x+b)q_w}{k_o(T_w - T_\infty)}$	Nusselt parameter
$Sh_x = -\frac{(x+b)j_w}{C_w - C_\infty}$	Sherwood parameter
$K(x)$	Permeability